Energy &
Environmental
Science

rsc.li/ees

Volume 11
Number 4
April 2018
Pages 719-1000

ISSN 1754-5706

ROYAL SOCIETY
OF CHEMISTRY

REVIEW ARTICLE
Yuekun Lai, Zhiqun Lin et al.
Graphene aerogels for efficient energy storage and conversion

ROYAL SOCIETY
OF CHEMISTRY

rsc.li/ees

Broader context

The global transition towards sustainable energy and electrified transportation is dependent on the development of next-generation energy storage systems with higher energy densities than current lithium-ion technology. Anode-free lithium metal batteries, which eliminate the conventional graphite anode and excess lithium, offer a promising solution for high-capacity storage. However, their cycle life is limited by rapid depletion of active lithium due to irreversible side reactions. A crucial approach is to develop a robust solid electrolyte interphase (SEI) to enable uniform lithium deposition and stripping, though this poses significant challenges. Additionally, ether-based electrolytes, though suitable for anode-free designs, tend to decompose at high voltages. It is also necessary to create a stable cathode-electrolyte interphase (CEI) that can reduce side reactions and expand the electrochemical window. This study presents an effective strategy using surface modification through HCMASS. This method guides electrolyte ion migration during formation, enriching anions in the solvation sheaths of lithium ions. This process results in a robust SEI with an ordered inorganic skeleton infused by organic components, exhibiting exceptional mechanical strength and high ionic permeability. Notably, HCMASS also optimizes the CEI layer, enabling stable operation of NCM811 cathodes in ether-based electrolytes. This coordinated regulation of both interfaces allows a 2.45 Ah anode-free Cu||NCM811 battery to achieve an energy density over 453.5 Wh kg^{-1}.

Helical Counter-Directional Migration-Induced Solvation Sheath Constructing Reinforced Electrode-Electrolyte Interphases for Ultra-Stable Anode-Free Lithium Metal Batteries

Yunyi Chen[1,2,3], Xitang Qian[1,2], Yuxiang Lyu[1,2], Yican Qiu[1,2], Yee Tung Kwan[1], Siyu Zhou[1,2], Xinyi Lan[1,2], Siqi Lu[1,2], Minhua Shao[1,2,3,4]*

1. Department of Chemical and Biological Engineering, The Hong Kong University of Science and Technology, Kowloon, Hong Kong 999077, China.

2. Energy Institute, The Hong Kong University of Science and Technology, Clear Water Bay, Kowloon, Hong Kong 999077, China.

3. Guangzhou Key Laboratory of Electrochemical Energy Storage Technologies, Guangzhou HKUST Fok Ying Tung Research Institute, Guangzhou 511458, China.

4. CIAC-HKUST Joint Laboratory for Hydrogen Energy, The Hong Kong University of Science and Technology, Clear Watery Bay, Kowloon, Hong Kong 999077, China.

5. *Corresponding to email: kemshao@ust.hk

Abstract

Anode-free lithium metal batteries hold great promise for high-capacity energy storage by eliminating both the conventional graphite anode and any excess lithium metal. However, irreversible charge-discharge cycles lead to the rapid depletion of active lithium inventories. Moreover, the ether-based electrolytes suited for anode-free configuration are unstable at high voltages, which makes them incompatible with high-nickel cathodes and ultimately curtails their role in enhancing energy density. This study proposes an interface modification strategy driven by helical counter migration. During the formation process, ion movement pathways and anions-cations association effects regulated by internal force generated by a magnetized nickel-coated current collector synergistically guide anions into solvation structures of the adjacent lithium ions migrating in the opposite direction, thereby forming a mechanically robust ion-permeable solid electrolyte interphase, which is characterized by an ordered inorganic particle skeleton infused with organic components, similar to the structure of reinforced concrete. Consequently, the helical counter-directional migration-assisted copper electrode achieves a coulombic efficiency of 99.9%. The assembled anode-free Cu||LiFePO$_4$ cell maintains over 80% capacity retention after 200 cycles, and the anode-less Cu||LiFePO$_4$ cell sustains stable operation for over 1,000 cycles. Furthermore, the internal electric field drives helical counter-directional migration-induced anion-derived solvation sheaths to diffuse to the cathode side and optimize the cathode-electrolyte interphase, enabling stable operation of high-nickel cathodes. The anode-free Cu||NCM811 cells cycled at 4.5 V exhibit a capacity retention exceeding 75% after 100 cycles, and realize a 453.5 Wh kg^{-1} anode-free lithium metal pouch cell configuration.

1 Introduction

Lithium metal anodes, boasting a theoretical specific capacity (3860 mAh g^{-1}) tenfold higher than graphite anodes, are recognized as a key anode candidate for achieving theoretical energy densities exceeding 500 Wh kg^{-1}.[1, 2] Adopting an anode-free configuration can maximize the advantages of lithium metal batteries. However, the formation of dendrites and isolated lithium caused by non-uniform lithium-ion aggregation are prone to continuous loss of active lithium and severe safety concerns,[3, 4] thus posing a key technical obstacle to the development of high energy density anode-free lithium metal batteries (AFLMBs).[5-7]

Research has shown that optimizing the electrode-electrolyte interphases can effectively regulate lithium-ion distribution and mitigate active lithium depletion.[8-10] Strategies include employing functional additives to enhance solid-electrolyte interphase (SEI) composition for improved lithium-ion diffusion kinetics,[11-13] or constructing artificial protective layers (via in-situ/ex-situ methods) to reinforce interfacial mechanical strength against vertical dendrite propagation.[14-16] Despite these advancements, complete suppression of the heterogeneous nucleation and growth of lithium remains elusive. Fundamental improvements require addressing the root mechanisms of the formation of non-uniform deposition structures such as dendrites and rods. Our previous studies reveal that the non-uniform lithium ion flux caused by the anisotropy of SEI is the main driving factor for dendrites/rods formation.[17] Although we have previously utilized external physical fields to achieve uniform interfacial lithium distribution,[18-20] the SEI remain susceptible to volume changes during charge/discharge cycles under anode-less conditions, trapped in a detrimental cycle of "fracture–reformation–fracture". Additionally, ether-based electrolytes, which are generally suitable for anode-free configurations, are prone to decomposition when operated at high-voltage. It is also necessary to find a suitable strategy to simultaneously construct a cathode-electrolyte interphase (CEI) that can suppress persistent side reactions to help broaden the electrochemical window.

In this work, we present a tailored helical counter-directional migration-induced anion-derived solvation sheaths (HCMASS) for the concurrent optimization of SEI and CEI structure and composition (Fig. 1). The non-uniform electrode surface induces curvature in the electric field distribution, attracting deflection in the migration trajectories of electrolyte cations/anions. A magnetized nickel layer coated on copper foil causes the ions to move at an angle relative to the magnetic field vector, resulting in a helical motion driven by an external force. Interestingly, anions tend to infiltrate the solvation structures of adjacent lithium ions while displacing neutral solvent molecules, thereby forming the HCMASS. These aggregated HCMASS preferentially form inorganic cluster nuclei at the current collector surface, subsequently interconnected by solvent reduction-derived organic components to create a reinforced steel-concrete-like mechanically robust ion-permeable SEI (MRIP-SEI) (Fig. 1b). In-situ Raman spectroscopy verifies that the magnetized nickel (M-Ni) coating regulates interfacial solvation structures and strong anion adsorption characteristics. Characterization techniques, including depth-profiling X-ray Photoelectron Spectroscopy (XPS), Time-of-Flight Secondary Ion Mass Spectrometry (ToF-SIMS), and Cryogenic Transmission Electron Microscopy (Cryo-TEM), validate the unique composition and architecture of this engineered SEI. Compared with conventional mosaic-type SEI, this hybrid structure demonstrates superior ionic conductivity and mechanical resilience, attributed to inorganic fillers providing structural support while organic binders enable elastic deformation. The organic-inorganic phase boundaries facilitate rapid lithium-ion transport, as evidenced by comprehensive electrochemical analysis. The HCMASS-assisted current collector achieves an exceptional coulombic efficiency (CE) of 99.9% at 1 mA cm^{-2}. When implemented in anode-less full cells (Negative/Positive capacity ratio=0.8), stable cycling over 1000 cycles is maintained with >80% capacity retention. Notably, the internal electric field (IEF) during discharge process drives the HCMASS to diffuse to the cathode side and optimize the cathode-electrolyte interphase, forming a protective layer that combines robust mechanical

properties with high lithium-ion conductivity, inhibiting the transition-metal dissolution (Fig. 1c). The innovation allows stable operation of $LiNi_{0.8}Co_{0.1}Mn_{0.1}O_2$ (NCM811) cathode materials while maintaining structural integrity. This advancement enables the anode-free Cu‖NCM811 pouch cell (~2.45 Ah) configuration to deliver an energy density of 453.5 Wh kg^{-1}. This work provides fundamental insights into HCMASS-assisted SEI engineering and demonstrates a practical pathway toward high-energy-density AFLMBs.
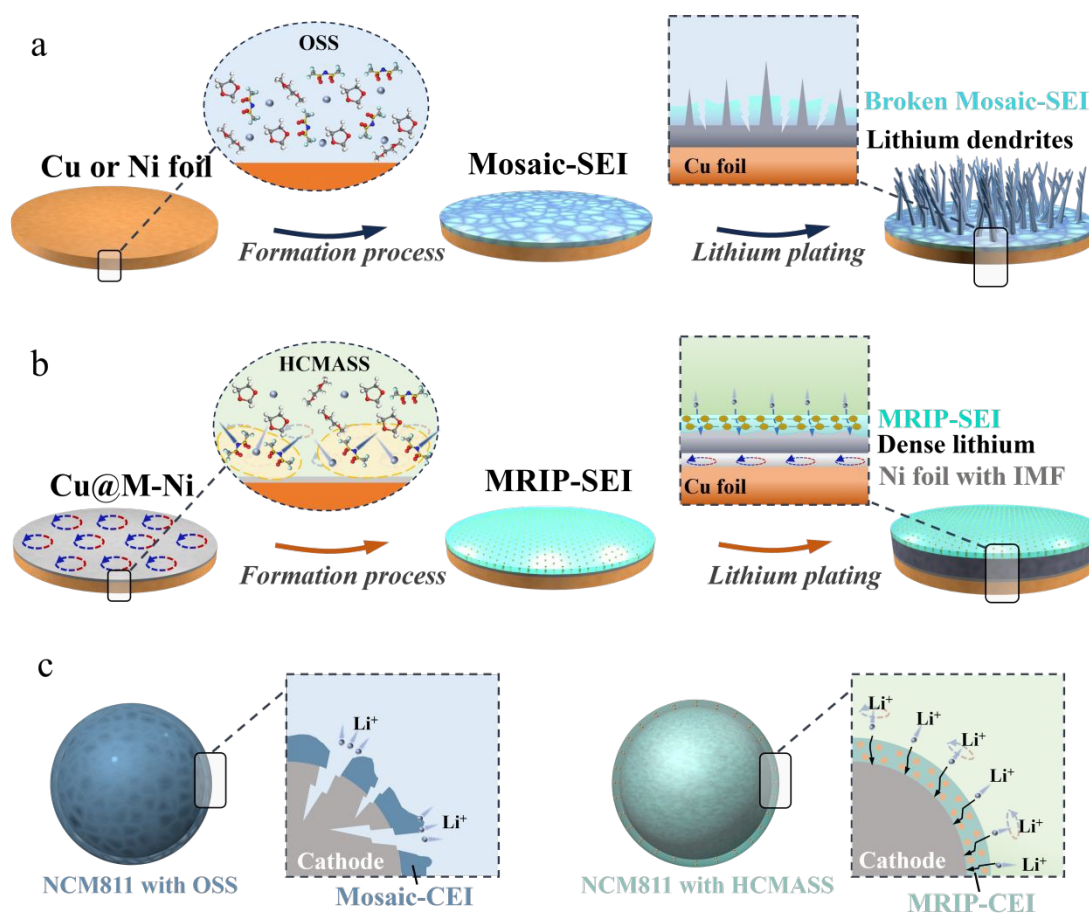
Fig. 1 Magnetized nickel-layer-induced HCMASS facilitating uniform lithium deposition. Schematic of lithium plating behavior on (a) Cu or Ni foil and (b) M-Ni coating. (c) Insertion and extraction behaviors of lithium ions in NCM811 with or without M-Ni coating.

2 Results and Discussion

2.1 Regulation of the solvation structure by the magnetized nickel layer to form HCMASS

In conventional ether-based electrolyte systems, lithium ions interact with anions and solvent components, resulting in the formation of an ordinary solvation sheath

structure (OSS) composed of solvent-anion complexes (Fig. 2a).[21] This solvation sheath

diffuses alongside Li$^+$ and preferentially undergoes reduction upon contact with the

anode surface, leading to the formation of a mosaic-structured SEI.[22, 23] This study

introduces an internal Lorentz force (ILF) through magnetized nickel-coated foils. The

inherent surface heterogeneity of electrodes induces electric field curvature, creating an

angular relationship between the motion trajectories of charged Li$^+$/TFSI$^-$ species and

the magnetic field direction.[24] ILF-driven counter-rotational dynamics facilitate anion

penetration into adjacent Li$^+$ solvation sheaths, ultimately forming HCMASS, as shown
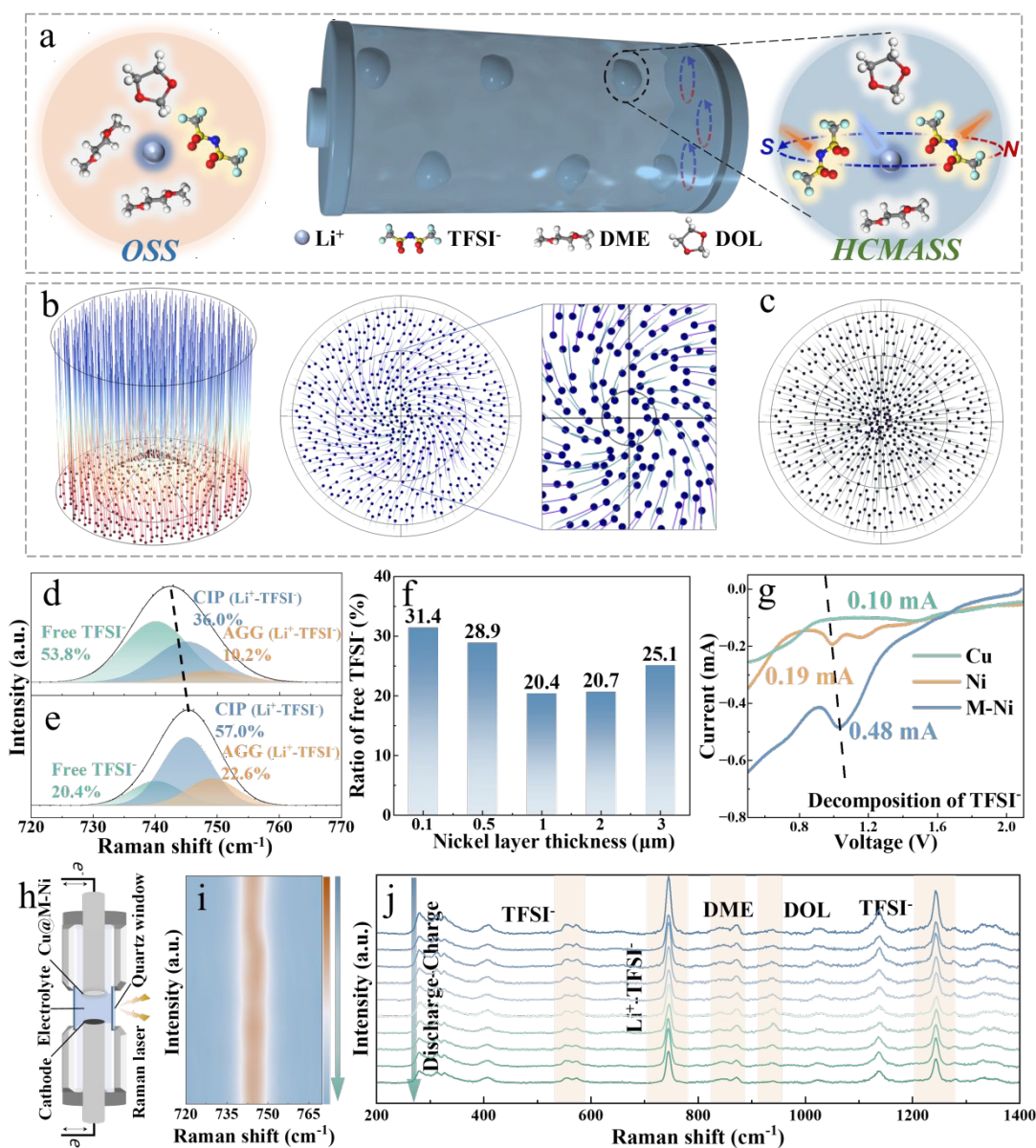
in Fig. 2a.

Fig. 2 Li$^+$ solvation structure under the action of M-Ni layer. (a) Schematic diagram of the

solvation structures on copper and non-magnetized nickel foil surfaces (Yellow), as well as those on magnetized nickel foil surfaces (Blue). Simulation results of the different trajectory of Li^+ during ions diffusion process (b) with M-Ni and (c) Ni or Cu. Raman spectra of $TFSI^-$ with (d) Ni and (e) M-Ni. (f) The proportion of free $TFSI^-$ in the solvated sheath under different magnetized nickel layer thickness conditions. (g) LSV curves of Li||Cu cells with various current collectors. (h) Schematic diagram of in-situ Raman test cell. (i) In-situ Raman spectra of Li^+-$TFSI^-$ during cycles with M-Ni. (j) In-situ Raman curves during charging/discharging cycles with M-Ni.

COMSOL simulations were employed to confirm the helical motion of ions near the anode surfaces. As shown in Fig. 2b, the paths of charged particles deflect under the influence of the ILF, resulting in the reconstruction of the original solvation structure. In contrast, such behavior is not observed in the control case (Fig. 2c). Furthermore, to validate that this helical motion promotes the entry of anions into the solvation sheath of Li^+ ions moving in the opposite direction, molecular dynamics (MD) simulations and in-situ Raman spectroscopy were used to investigate the ether-based electrolyte chemistry with different conditions. The radial distribution functions (RDF) and coordination numbers (CNs) of Li^+-O ($TFSI^-$) are derived from MD simulations to explore the coordination of Li^+ with and without ILF (Fig. S1, Supporting Information). After applying an ILF in the simulation system, both the height and area of the first peak in the RDF increase, suggesting a rise in the CNs of $TFSI^-$ around the Li^+. By integrating the g(r)-r plot, the variation of CNs with r is obtained, as shown in Fig. S1a-1c, Supporting Information. Further calculations reveal that under the influence of ILF, the Li^+-O($TFSI^-$) coordination number increases from 1.73 to 2.12 (Fig. S1d, Supporting Information). This indicates that spiral migration leads to more anions entering the solvation sheaths of adjacent lithium ions moving in the opposite direction. Raman spectroscopy was also used to explore the solvation sheaths. Quantitative analysis reveals distinct $TFSI^-$ participation ratios in solvation structures: 26.7% for Cu foil, 46.2% for Ni-coated electrodes, and enhanced 79.6% under M-Ni configuration (Fig. 2d,e; Fig. S2, Supporting Information), demonstrating strengthened cation-anion association. This conclusion is consistent with the results obtained from Fourier transform infrared (FTIR) spectroscopy (Fig. S3, Supporting Information). A

systematic investigation was conducted to examine the effects of nickel layer thickness and magnetic flux density on lithium-ion/anion coordination. Through electrodeposition of nickel layers (0.1-3 μm thickness range) on Cu foil followed by 180 days magnetization achieving 5-15 mT flux density (Fig. S4 and S5, Supporting Information), Raman spectroscopy reveals an optimal TFSI$^-$ coordination trend. The coordination between Li$^+$ and anions progressively enhances as the nickel thickness increased from 0.1 μm (5 mT) to 1 μm (10 mT). However, further thickness increases (1-3 μm, 10-15 mT) result in coordination decline due to electrostatic interactions (Fig. 2f; Fig. S6, Supporting Information). Comprehensive electrochemical testing and morphological characterization on current collectors with varying nickel thicknesses after formation demonstrates that Li||Cu@Li cells with 1μm-thick nickel layers achieve the most favorable performance metrics: lowest interfacial impedance (45.7 Ω), highest CE (99.9%), and densest lithium deposition morphology (Fig. S7-S9, Supporting Information). Therefore, a nickel layer thickness of 1 μm is selected as the optimal choice for subsequent studies. These findings indicate that the optimized HCMASS creates an advantageous interfacial microenvironment for lithium plating/stripping processes.

HCMASS also demonstrates an enhanced capability to induce anion decomposition at the interface, as confirmed by linear sweep voltammetry (LSV) measurements. The TFSI$^-$ decomposition current on the M-Ni surface reaches 0.48 mA, higher than those observed on Cu foil (0.10 mA) and non-magnetized Ni layer (0.19 mA) (Fig. 2g). Furthermore, the reduction potential of TFSI$^-$ on M-Ni exhibits an anodic shift, indicating more favorable decomposition kinetics under these conditions. To validate the stability of HCMASS induced by the M-Ni coating, we designed an electrochemical cell for in-situ Raman spectroscopy monitoring during galvanostatic cycling (Fig. 2h). The persistent Li$^+$-TFSI$^-$ interaction is evidenced by the stable Li$^+$-TFSI$^-$ Raman shifts at 745 cm^{-1} throughout cycling, suggesting the dominance of contact ion pairs (CIPs) in the solvation structure (Fig. 2i). Both solvent molecules and

anions maintain stable Raman signatures during charge/discharge processes, confirming the exceptional stability of HCMASS (Fig. 2j). In contrast, OSS exhibits inferior stability with dynamic Free-DOL characteristics (~730 cm^{-1}) showing cycle-dependent "appearance-disappearance-decay" behavior (Fig. S10, Supporting Information). This indicates interfacial instability that may lead to anisotropic composition, structure, and properties in OSS-derived SEI layers[25].

2.2 Optimizing SEI layer composition and structure through HCMASS

The HCMASS can help facilitate interfacial generation of abundant inorganic constituents through anion-dominated solvation sheaths. These inorganic components aggregate into uniformly distributed nanoparticles under interfacial micro-magnetic field effects, as jointly validated by Cryo-TEM (Fig. S11, Supporting Information), XPS depth profiling, and ToF-SIMS. Firstly, Cryo-TEM shows the HCMASS-induced MRIP-SEI demonstrates superior uniformity with ~25 nm thickness satisfying electron tunneling suppression criteria[26] (Fig. 3a), while OSS-derived SEI exhibits irregular undulating morphology with thickness fluctuations (Fig. 3b), detrimental to homogeneous Li$^+$ transport. High-resolution Cryo-TEM imaging reveals inorganic substances in the MRIP-SEI are assembled into ~2-4 nm particles with ordered alignment, forming a robust "reinforced concrete-like" SEI architecture (Fig. 3c). In contrast, OSS-SEI displays amorphous characteristics corresponding to organic-rich interfacial layers (Fig. S12a, Supporting Information). Through calibration of surface-proximal lattices in Cryo-TEM images and measurement of lattice spacings in inverse fast Fourier transform (FFT) patterns (Fig. 3d; Fig. S13, Supporting Information), it is identified that abundant inorganic components in MRIP-SEI including LiF (111), LiF (200), Li$_2$S (200), and Li$_2$O (111) (Table S1, Supporting Information). These findings corroborate our proposed MRIP-SEI formation mechanism: Anion-aggregated solvation sheaths preferentially react to generate inorganic species that coalesce into nanoparticles under magnetic field guidance, subsequently interconnected by organic byproducts from solvent reduction, ultimately forming a LiF-rich inorganic-organic

interfacial passivation layer with an ordered structure. Selected area electron diffraction (SAED) patterns confirm polycrystalline features with concentric rings corresponding to LiF, Li_2O, Li_3N, and Li_2S phases (Fig. 3e). To assess the structural stability of the SEI, we systematically characterized lithium morphologies post-cycling on different substrates. The interfacial passivation layers on conventional Cu foils show indistinguishable structural features (Fig. S12b, Supporting Information), likely due to uneven lithium deposition/stripping behaviors that severely compromise the fragile OSS-SEI layers. Conversely, MRIP-SEI maintains its dense outer structure with preserved original morphology even after multiple lithium-ion transits (Fig. S12c, Supporting Information). Lattice calibration and FFT pattern analysis of MRIP-SEI after cycling (Fig. S14, Supporting Information) confirm persistent retention of inorganic components after prolonged cycling.

The XPS spectra of F 1s consistently exhibit a prominent peak at 685 eV binding energy throughout the SEI layer (Fig. 3f), indicating a high inorganic content of LiF.[27] Time-resolved sputtering analysis reveals fluorine maintains dominant proportions (45-50%) across the SEI thickness, exceeding other elemental ratios, confirming LiF-rich SEI formation (Fig. 3g). The LiF fraction in F 1s spectra reaches 95.2%, 44.5%, and 17.4% for M-Ni, non-magnetized Ni, and Cu foils, respectively (Fig. S15a-c, Supporting Information). Furthermore, HCMASS promotes interfacial generation of additional inorganic phases including Li_3N and Li_2O (Fig. 3h; Fig. S15d, Supporting Information). In contrast, conventional non-magnetized Ni and Cu foils develop SEI layers predominantly composed of organic constituents with minimal LiF, Li_2O, or Li_3N content (Fig. S15e-g, Supporting Information). Remarkably, the HCMASS-induced SEI demonstrates exceptional stability, retaining original MRIP-SEI composition with substantial LiF, Li_2O, and Li_3N components even post-cycling (Fig. S16, Supporting Information).
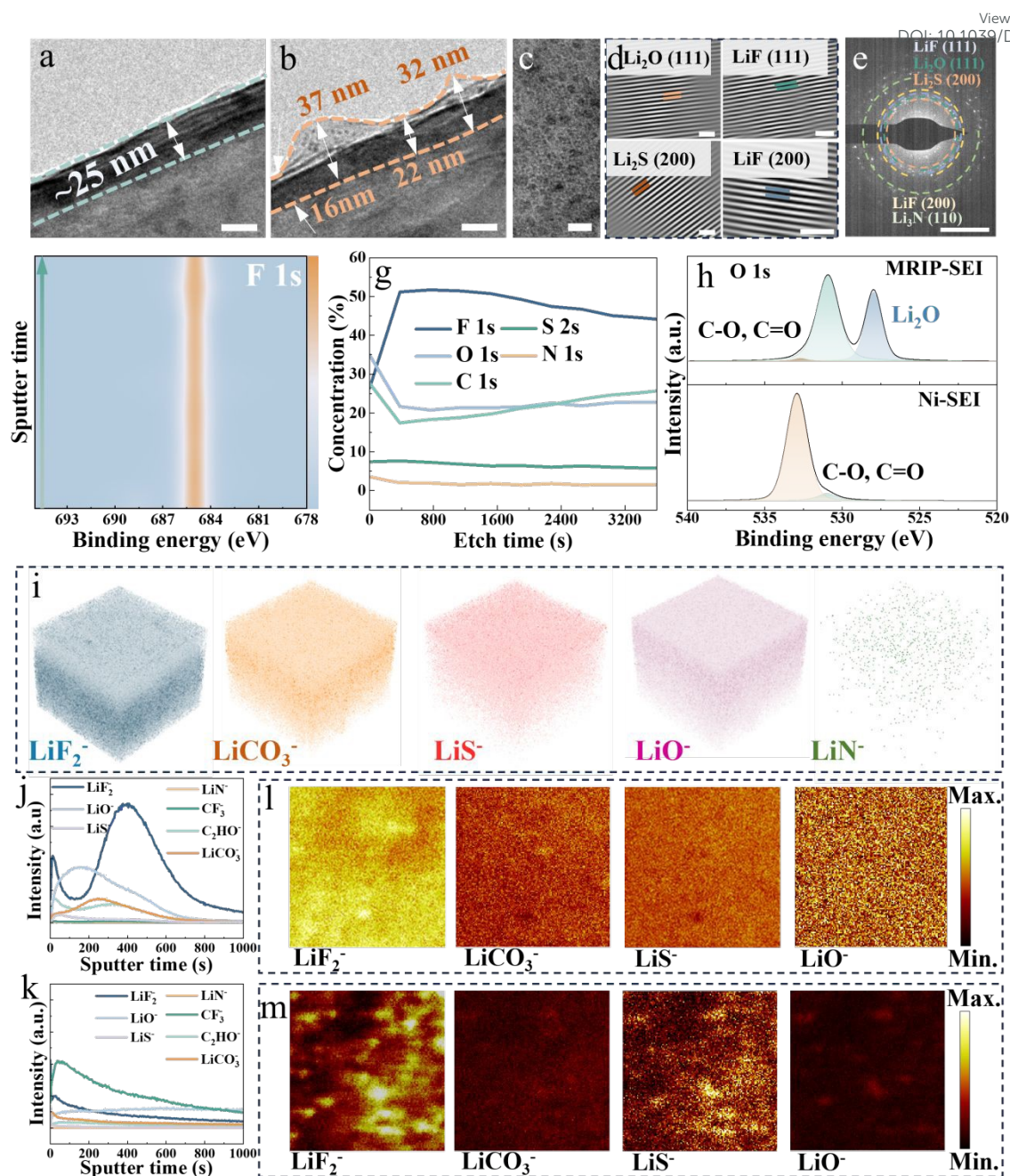
Fig. 3 Composition distribution of MRIP-SEI layer induced by HCMASS. Cryo-TEM images of (a) MRIP-SEI (M-Ni) and (b) Ni-SEI morphologies (Scale bar: 20 nm). (c) High-resolution Cryo-TEM images of the MRIP-SEI (Scale bar: 5 nm). (d) Inverse FFT images of MRIP-SEI (Scale bar: 1 nm). (e) SAED pattern of the regions at the surface of growth lithium (Scale bar: 5 1/nm). (f) High-resolution XPS spectra depth-profiles of the formed MRIP-SEI (M-Ni) of F 1s. (g) The atomic composition ratios of MRIP-SEI varying with sputter time. (h) XPS spectra of O 1s of MRIP-SEI and Ni-SEI. (i) TOF-SIMS 3D distribution of MRIP-SEI (M-Ni). Depth profiles of (j) MRIP-SEI and (k) Ni-SEI. Single-color gradient maps of LiF_2^-, $LiCO_3^-$, LiS^-, and LiO^- in (l) MRIP-SEI and (m) Ni-SEI.

Three-dimensional ToF-SIMS mapping elucidates the structural hierarchy and spatial distribution of SEI components. The MRIP-SEI exhibits higher concentrations

of LiF and inorganic constituents compared to conventional SEI, particularly enriched in the middle and lower layers, which form a robust passivation architecture (Fig. 3i). Conversely, OSS-induced SEIs on non-magnetized Ni and Cu foils displays complex organic-inorganic hybrids with predominant organic content (Fig. S17 and S18, Supporting Information). These organic components demonstrate limited passivation effectiveness, leaving the electrode-electrolyte interphases susceptible to persistent parasitic reactions.[28] Depth-resolved elemental mapping confirms LiF_2^- dominance in MRIP-SEI, aligning with XPS sputtering trends (Fig. 3j and k). Monochromatic gradient plots of LiF_2^-, LiO^-, LiS^-, and $LiCO_3^-$ species reveal homogeneous inorganic distribution in MRIP-SEI, facilitating isotropic Li^+ diffusion channels and superior deposition morphology (Fig. 3l). In stark contrast, OSS-SEI on non-magnetized Ni and Cu foils shows a highly heterogeneous distribution of these inorganic components, promoting selective Li^+ diffusion/deposition that fosters dendrite growth and the formation of "dead lithium" (Fig. 3m; Fig. S19, Supporting Information). These findings establish M-Ni's critical role in stabilizing LiF-rich SEI formation and enabling reversible electrochemical processes.

2.3 MRIP-SEI with both high lithium ions conductivity and strong mechanical properties

As illustrated in Fig. 4a, in the ordered inorganic-organic composite MRIP-SEI, the abundant inorganic clusters provide the SEI layer with superior mechanical properties to ensure structural integrity, while the uniform organic-inorganic spatial arrangement facilitates the construction of rapid lithium-ion diffusion pathways. The interfacial impedance of this structure is lower than that of organic-derived SEI and completely passivated inorganic SEI (Fig. S20, Supporting Information). To systematically elucidate the superior performance of HCMASS-induced MRIP-SEI in lithium-ion transport, interfacial kinetics, and mechanical stability, comprehensive electrochemical characterizations were conducted. The activation energy (E_a) for Li^+ migration across the SEI interface was quantitatively determined through temperature-

dependent electrochemical impedance spectroscopy (EIS) analysis.[14] The Nyquist plots

acquired at varying temperatures (30-60°C) consistently demonstrates lower interfacial

resistance (R_{in}) for MRIP-SEI compared to conventional Ni-SEI and Cu-SEI systems

across all tested temperatures (Fig. 4b-d; Fig. S21a,b, Supporting Information). This

performance enhancement originates from the unique reinforced concrete-like

architecture that effectively suppresses parasitic side reactions while establishing
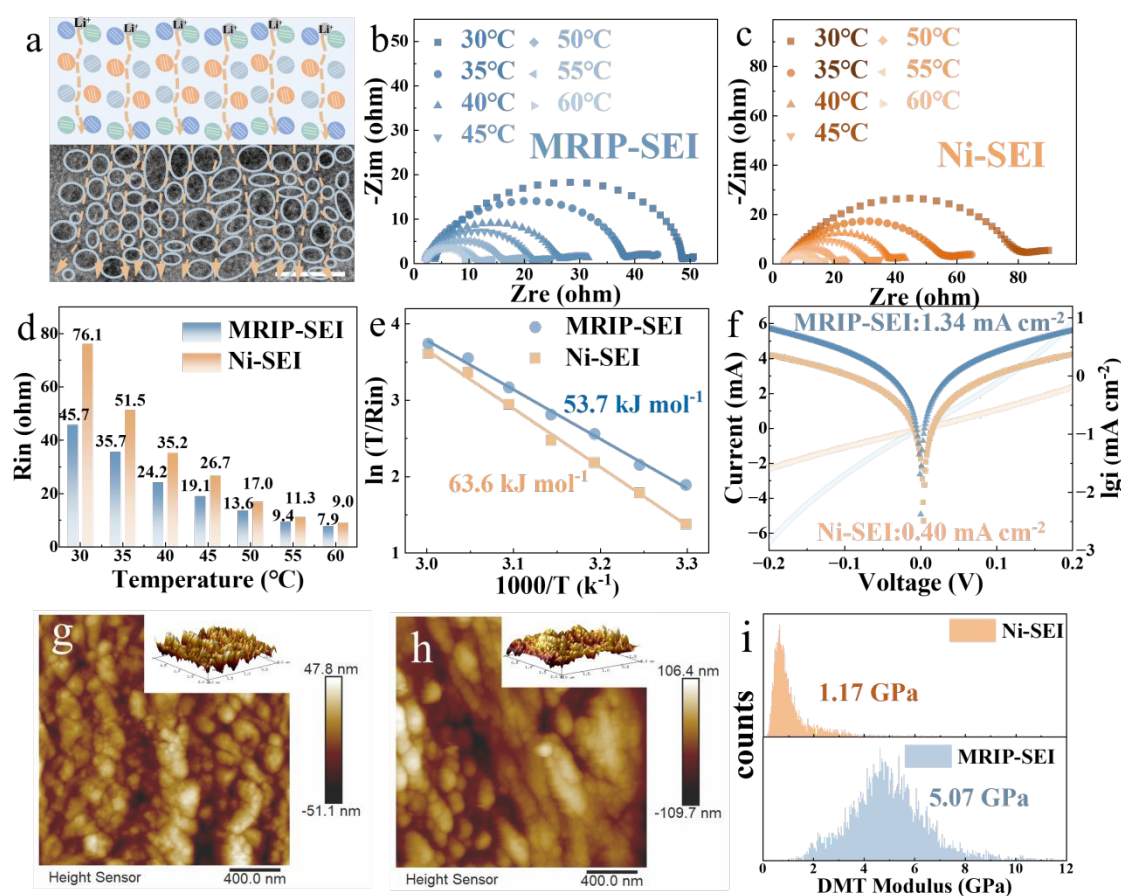
efficient ion-conducting channels.

Fig. 4 properties of SEIs. (a) Schematic diagram and Cryo-TEM image of the interfacial structure and lithium ions diffusion path in MRIP-SEI (Scale bar: 10 nm). EIS after the generation of (b) MRIP-SEI and (c) Ni-SEI at seven different temperatures (30, 35, 40, 45, 50, 55, 60 °C). (d) Impedance comparison of MRIP-SEI and Ni-SEI. (e) The activation energy for ion diffusion in SEI layers. (f) Tafel plots and corresponding exchange current of MRIP-SEI and Ni-derived SEI. AFM images of the current collectors' surfaces with (g) MRIP-SEI and (h) Ni-SEI. (i) DMT modulus distribution of MRIP-SEI and OSS-derived Ni-SEI.

Arrhenius analysis of temperature-dependent E_a values reveals a reduced diffusion

barrier (activation energy) for MRIP-SEI (53.7 kJ mol⁻¹) compared to Ni-SEI (63.6 kJ

mol^{-1}) and Cu-SEI (76.0 kJ mol^{-1}), providing mechanistic insight into its enhanced Li transport efficiency (Fig. 4e; Fig. S21c, Supporting Information). Complementary Tafel analysis derived from cyclic voltammetry (CV) measurements was used to quantify the interfacial charge transfer kinetics, with exchange current density (j_0) values calculated from polarization curves (Fig. 4f; Fig. S21d, Supporting Information). The MRIP-SEI exhibits exceptional j_0 values of 1.34 mA cm^{-2}, outperforming Ni-SEI (0.40 mA cm^{-2}) and Cu-SEI (0.31 mA cm^{-2}), confirming superior charge transfer capability and sufficient lithium flux for homogeneous deposition.

The mechanical reinforcement provided by MRIP-SEI was systematically investigated through nanomechanical characterization. Atomic Force Microscopy (AFM) 3D topography reveals a more homogeneous surface morphology with reduced roughness compared to conventional SEI layers (Fig. 4g and 4h; Fig. S22a, Supporting Information), suggesting favorable conditions for uniform lithium nucleation. Quantitative Derjaguin-Muller-Toporov (DMT) modulus analysis derived from stress-displacement curves demonstrated remarkable mechanical enhancement, with MRIP-SEI exhibiting an average modulus of 5.07 GPa versus 1.07 GPa (Ni-SEI) and 0.99 GPa (Cu-SEI) (Fig. 4i; Fig. S22b, Supporting Information). This mechanical superiority stems from the ordered inorganic-dominated architecture that functions as a strain-resistant shield during repeated lithium plating/stripping cycles.[29]

2.4 HCMASS-induced MRIP-SEI for optimizing the behavior of lithium plating

Although previous studies have confirmed the regulatory role of external physical fields on lithium deposition behavior, a key challenge remains in developing straightforward methods for integrating external forces directly at electrode-electrolyte interphases.[18] In this study, we comprehensively validated the effectiveness of MRIP-SEI through a multi-modal approach combining scanning electron microscopy (SEM), focused ion beam-SEM (FIB-SEM), in-situ optical microscopy, and multi-physics simulations. The experimental protocol consisted of subjecting the cell to a single charge-discharge cycle to form the SEI, followed by lithium deposition at 0.1 mA cm$^-$

^{2} to 0.15 mAh cm^{-2}. FIB-SEM characterization reveals that HCMASS-derived MRIP-SEI induces exceptionally dense lithium deposition approaching theoretical limits (~0.73 μm) (Fig. 5a-b). In contrast, Ni-SEI system exhibits pronounced void formation (Fig. 5c), attributed to structural and compositional heterogeneity triggering regional selective plating.
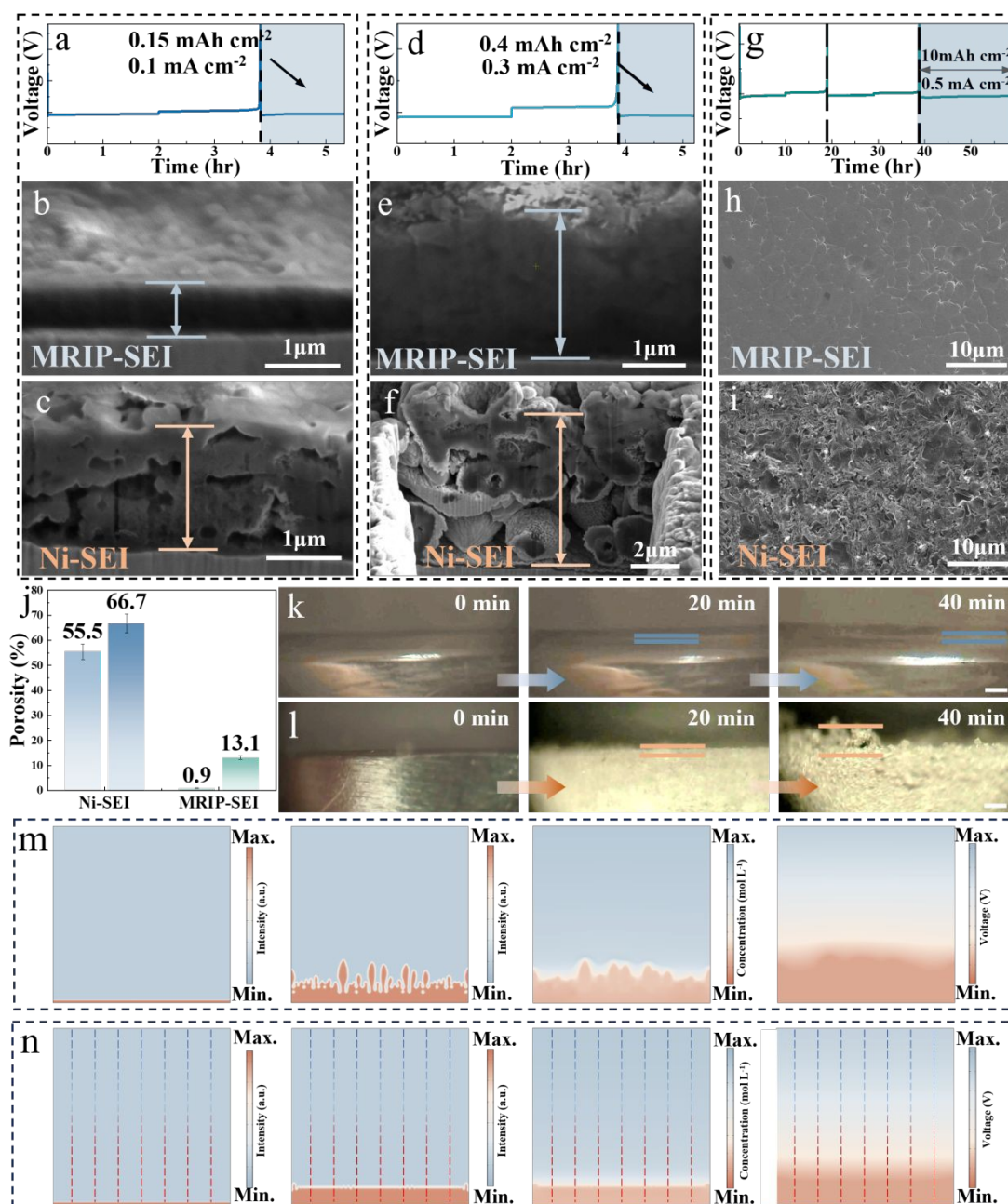

Fig. 5 Deposition behaviors on various current collectors. (a) Charge/discharge profiles and corresponding FIB-SEM images with (b) MRIP-SEI and (c) Ni-SEI at 0.1 mA cm^{-2}. (d) Charge/discharge profiles and corresponding FIB-SEM images with (e) MRIP-SEI and (f) Ni-SEI at 0.3 mA cm^{-2}. (g) Charge/discharge profiles and corresponding SEM images with (h)

15

MRIP-SEI and (i) Ni-SEI at 0.5 mA cm⁻². (j) Comparison of porosity of lithium deposition layers induced by different current collectors. Morphological evolution of electrodeposited Li characterized by real-time optical microscopy with (k) MRIP-SEI and (l) Ni-SEI. Phase field simulation results of lithium deposition induced by (m) heterogeneous nucleation (Ni-SEI) and (n) uniform nucleation (MRIP-SEI).

When subjected to increased current density (0.3 mA cm⁻²) and areal capacity (0.4 mAh cm⁻²), the MRIP-SEI preserves structural integrity while demonstrating void-free lithium deposition, with the deposited layer thickness reduced to one-third of control samples (Fig. 5d-f). Under extreme operational conditions (0.5 mA cm⁻², 10 mAh cm⁻²), MRIP-SEI effectively inhibits dendritic growth, in sharp contrast to Ni-SEI which develops hazardous rod-like protrusions prone to dead lithium formation during cycling (Fig. 5g-i). Quantitative characterization reveals remarkably low porosity levels in the M-Ni system: 0.9% (0.1 mA cm⁻²) and 13.1% (0.3 mA cm⁻²), which correlates with the reduced deposition layer thickness and indirectly confirms the exceptional ionic conductivity and mechanical resilience of MRIP-SEI. Comparatively, unmagnetized Ni foils exhibits higher average porosity values of 55.5% (0.1 mA cm⁻²) and 66.7% (0.3 mA cm⁻²) (Fig. 5j). Cross-sectional SEM analysis further highlights that the unoptimized solvation structure near Cu foils led to extensive void formation and dendritic crystallization (Fig. S23, Supporting Information). Post-charge/discharge-cycling SEM characterization demonstrates sustained densification of deposited layers enabled by MRIP-SEI (Fig. S24, Supporting Information), attributable to persistent high lithium-ion flux and maintained mechanical stability throughout charge-discharge processes.[30, 31]

In-situ optical microscopy further reveals distinct differences between MRIP-SEI and OSS-SEI. After plating at 2 mA cm⁻², the lithium metal with OSS-SEI exhibits numerous loose structures (Fig. 5l), whereas the deposition morphology in MRIP-SEI system shows no significant heterogeneous accumulation layer (Fig. 5k). These observations align with FIB-SEM results. COMSOL Multiphysics simulations of phase field, concentration field, and potential field during lithium deposition reveal contrasting nucleation mechanisms (Fig. 5m,n; Fig. S25-S27, Supporting Information).

In the control case, lithium demonstrates stochastic and localized nucleation, primarily forming rod-like structures accompanied by chaotic concentration and potential distributions (Fig. 5m). While this represents an improvement over single-site deposition morphology, such heterogeneous deposition behavior remains challenging for achieving high efficiency and long-term cycling stability in anode-free cells. In contrast, the multi-site homogeneous nucleation process with MRIP-SEI (M-Ni) yields a dense lithium deposition morphology with minimal branching (Fig. 5n). This plating behavior closely resembles ideal uniform deposition, accompanied by stable lithium-ion concentration and potential distributions, highlighting the superior interfacial stability enabled by MRIP-SEI.

2.5 MRIP-SEI to optimize interfacial mass transfer for high-performance anode-free lithium metal batteries

The MRIP-SEI interfacial layer demonstrates remarkably enhanced electrochemical properties across multiple battery configurations. Lithium symmetric cells incorporating MRIP-SEI exhibit cycling stability exceeding 5000 hours at 2 mA cm^{-2}, outperforming conventional Ni-SEI and Cu-SEI systems by 12-fold and 20-fold, respectively (Fig. 6a; Fig. S28, Supporting Information). Notably, symmetric cells enabled by MRIP-SEI maintain a stable low overpotential of ±70 mV throughout cycling (Fig. 6b), indicating homogeneous lithium deposition and stripping. In contrast, Ni-SEI and Cu-SEI counterparts display progressively increasing and unstable overpotentials. From the comparison of FIB-SEM images, it can be seen that after cycling, the lithium plating layer induced by MRIP-SEI is still very dense and there are no large voids. In contrast, the lithium plating process under OSS-SEI is very uneven, with a large number of voids, which easily produces dead lithium and causes continuous loss of active lithium (Fig. 6c). To assess lithium cycling reversibility, Li||Cu half-cells were fabricated for CE measurements. The MRIP-SEI-based half-cells achieve over 1400 reversible cycles at 0.5 mA cm^{-2}, demonstrating 15-fold greater cycle longevity compared to Ni-SEI and Cu-SEI systems (Fig. 6d,e; Fig. S29 Supporting Information).

17

Particularly noteworthy is their sustained operation beyond 500 cycles at 1 mA cm^{-2} (Fig. S30, Supporting Information), coupled with an average CE of 99.8% at 2 mA cm^{-2} (Fig. 6f), establishing critical technical foundations for anode-free full-cell configurations. Compared with some previously reported literature, the Li||Cu half-cell exhibits longer cycle stability and higher average CE (Table S2, Supporting Information).

This performance superiority extends to anode-less Cu@Li||LFP full-cell configurations. The full cell dominated by the MRIP-SEI layer exhibits excellent stability, maintaining more than 80% capacity retention after 1000 cycles at 0.5C rate (N/P=0.8), while the cell with Ni-SEI layer shows rapid capacity decay starting from the 370th cycle. (Fig. 6g, Fig. S31, Supporting Information). Alarmingly, Cu-SEI-based lithium metal batteries suffer catastrophic capacity collapse, plunging below 60% retention after merely 45 cycles (Fig. S32, Supporting Information). Compared with the full lithium metal cells reported in recent literature, the ultra-stable cycling performance demonstrated in this work shows remarkable competitiveness in terms of long-term operational durability (Fig. S33, and detailed data can be found in Table S3, Supporting Information). Under anode-less conditions (N/P=0.3), MRIP-SEI-enabled cells preserve >85% capacity retention with a specific discharge capacity of 150 mAh g^{-1} through 300 cycles (Fig. 6h). In contrast, Ni-SEI systems display precipitous capacity degradation trajectories, collapsing to <20% retention within 100 cycles. Notably, under anode-free conditions (N/P=0), the capacity retention of Cu||LFP cell with MRIP-SEI is higher than 80% after 200 cycles, while the capacity of Cu||LFP cell with Ni-SEI and Cu-SEI decay to nearly 0 mAh after 70 and 60 cycles, respectively (Fig. 6i, and Fig. S34, 35, Supporting Information).
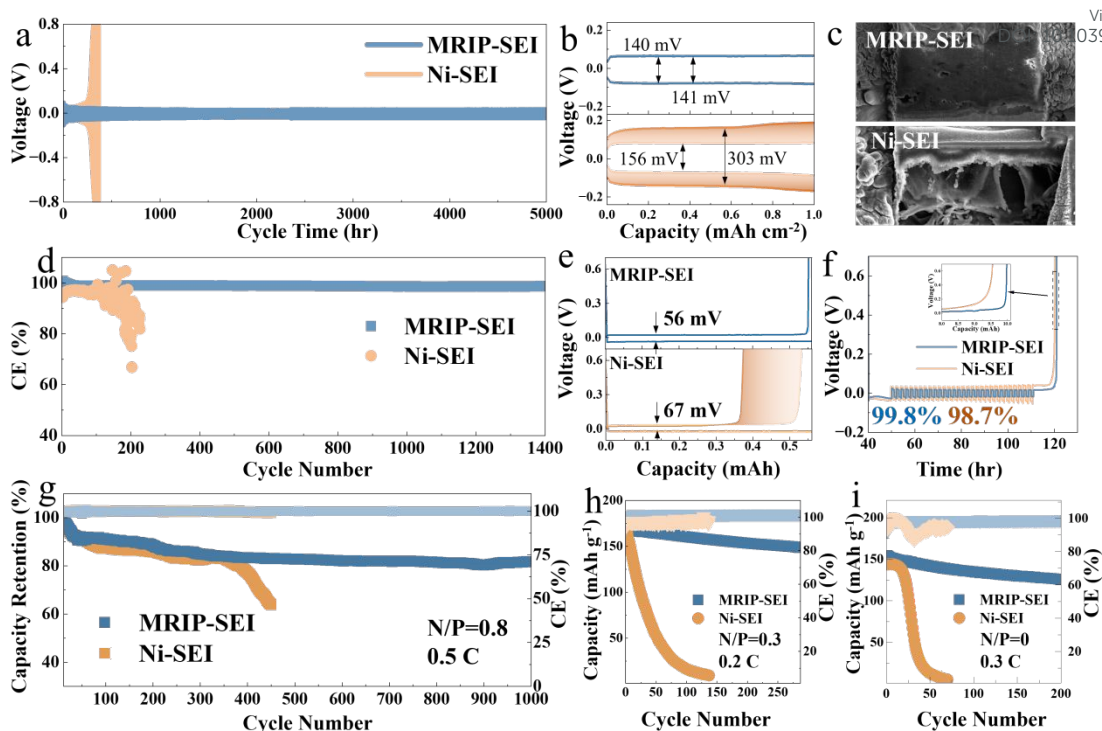
View Article Online
039/D5EE06208J

Fig. 6 MRIP-SEI to optimize interfacial mass transfer for high-performance anode-free and anode-less lithium batteries. (a) Comparison of cycling performance and (b) charging/discharging curves of Li‖Li symmetrical cells at 2 mA cm⁻². (c) FIB-SEM images with MRIP-SEI and Ni-SEI after cycling. (d) Comparison of cycle performance of Li‖Cu cells and (e) corresponding charging/discharging curves at 0.5 mA cm⁻². (f) Aurbach average CE of Li‖Cu cells at 2 mA cm⁻². (g) Cycling performance of Cu@Li‖LFP full cells at 0.5 C (N/P~0.8). (h) Cycling performance of anode-less Cu@Li‖LFP full cells at 0.2 C (N/P~0.3). (i) Cycling performance of anode-free Cu‖LFP full cells at 0.3 C (N/P=0).

2.5 Enhancing CEI by HCMASS for stable high-voltage anode-free Cu‖NCM811 batteries

Although ether-based electrolytes exhibit excellent compatibility with lithium metal anodes, their implementation in high-voltage NCM811 cathode systems is hindered by persistent parasitic reactions that accelerate capacity degradation. Our investigation reveals that HCMASS extends its interfacial optimization capabilities to the CEI through ILF and IEF driving during discharge process, forming a MRIP-CEI analogous to the MRIP-SEI (Fig. 1c). To verify whether HCMASS has accumulated on the cathode side, in-situ Raman was used to detect the real-time changes in the electrolyte solvation structure near the cathode surface. As shown in Fig. S36, the signals of the electrolyte near the cathode exhibits a strongest intensity at 745 cm⁻¹

19

Raman shift, indicating a strong interaction between anions and cations, which manifests as the presence of contact ion pairs (CIP) on the cathode side. Further detailed analysis of these peaks reveals that their intensity increases along with the charge/discharge cycling, suggesting a significant rise in the quantity of CIP. This trend may be attributed to the migration of lithium ions from the anode to the cathode during discharge, leading to the accumulation of HCMASS on the cathode side. Comparison of this Raman spectrum with that of an OSS shows a clear redshift from ~742 cm^{-1} to ~745 cm^{-1}, indicating that most of the anions near the cathode participates in the solvation structure of Li^+, forming HCMASS. Furthermore, in-situ Raman spectroscopy reveals a significant intensity change at a Raman shift of ~941 cm^{-1} (Fig. S36d, Supplementary Information). This relatively strong solvent peak observed during charging gradually weakened during discharging, indicating that HCMASS has a shielding effect on free solvents at both anode and cathode. To verify the universality of this strategy, HCMASS aggregation at the electrode-electrolyte interface is still observed in localized high concentration ether-based electrolyte (LHCEE) (Fig. S37, Supplementary Information). Therefore, the ILF generated by M-Ni not only affects the anode but also modulates the cathode interface environment by forming HCMASS in the electrolyte, demonstrating a certain degree of versatility. The accumulation of HCMASS on the cathode promotes the formation of anion-derived inorganic-rich CEI.

This dual-functional interphase not only suppresses electrolyte decomposition but also stabilizes the cathode structure during lithium intercalation/deintercalation. Cryo-TEM characterization demonstrates that MRIP-CEI induced by HCMASS maintains a uniform thickness of 10 nm (Fig. 7a), in stark contrast to the irregular OSS-derived CEI (5-39 nm thickness variations) (Fig. 7b), which promotes localized lithium-ion flux accumulation at thinner regions, ultimately inducing particle cracking. High-resolution Cryo-TEM imaging and selected-area electron diffraction (SAED) confirm the abundant presence of inorganic components such as LiF within MRIP-CEI (Fig. 7c,d), while XPS analysis quantitatively verifies its LiF-rich composition, providing essential

mechanical reinforcement (Fig. 7e; Fig. S38, Supporting Information). AFM characterization further confirms the interfacial strengthening effect of MRIP-CEI, and the DMT modulus of NCM811 particles under the protection of MRIP-CEI is 28.8 GPa, while that of NCM811 particles with OSS-derived CEI is only 5.6 GPa after cycling tests (Fig. 7f,g). Cryo-TEM and XPS analysis of the NCM811 material after cycling further reveals that the MRIP-CEI layer exhibits exceptional stability (Fig. S39 and S40, Supporting Information), retaining its original thickness and uniform structure (10 nm), while remaining abundant in LiF.

The LSV curves confirm that the CEI generated under the influence of M-Ni effectively slows down the oxidative decomposition of the electrolyte (Fig. S41, Supporting Information). The stable operating voltage window increases from approximately 4.0 V to around 4.5 V (vs. Li/Li$^+$), with the decomposition current remaining below 2.2 μA cm^{-2} (0.5 mV s^{-1}). In-situ EIS and distribution of relaxation times (DRT) techniques were performed to decouple specific electrochemical processes on a time scale. Tracking the relaxation time identifications helps reveal the electrode-electrolyte interphase chemistry during cycling. As shown in Figure 7h, τ1 at 10^{-5} s can be assigned to the contact resistance corresponding to the electrolyte resistance. In addition, the peaks τ2 (at 10^{-4} to 10^{-3} s) and τ3 (at 10^{-3} to 10^{-2} s) indicate the ions transport through the CEI/SEI layer. The DRT spectra show a peak at 10^{-2} s, corresponding to the charge transfer resistance (τ4), and the peaks (τ5, τ6) at 10^{-1} to 10 s indicate mass transfer. It is worth noting that in the control case (without M-Ni), obvious peaks are shown at τ2 and τ3 due to the large impedance of CEI and SEI. This high charge/discharge resistance between NCM811 and the electrolyte severely hinders the ion diffusion. In contrast, the NCN811 cell with M-Ni maintains a relatively low interfacial resistance, indicating that MRIP-CEI has fast lithium ions diffusion channels. This optimized ion transport pathway enables highly reversible lithium ions migration, and FIB-SEM confirms the structural integrity of the MRIP-CEI-protected cathode particles, while a large number of voids are formed in the unmodified cathode particles
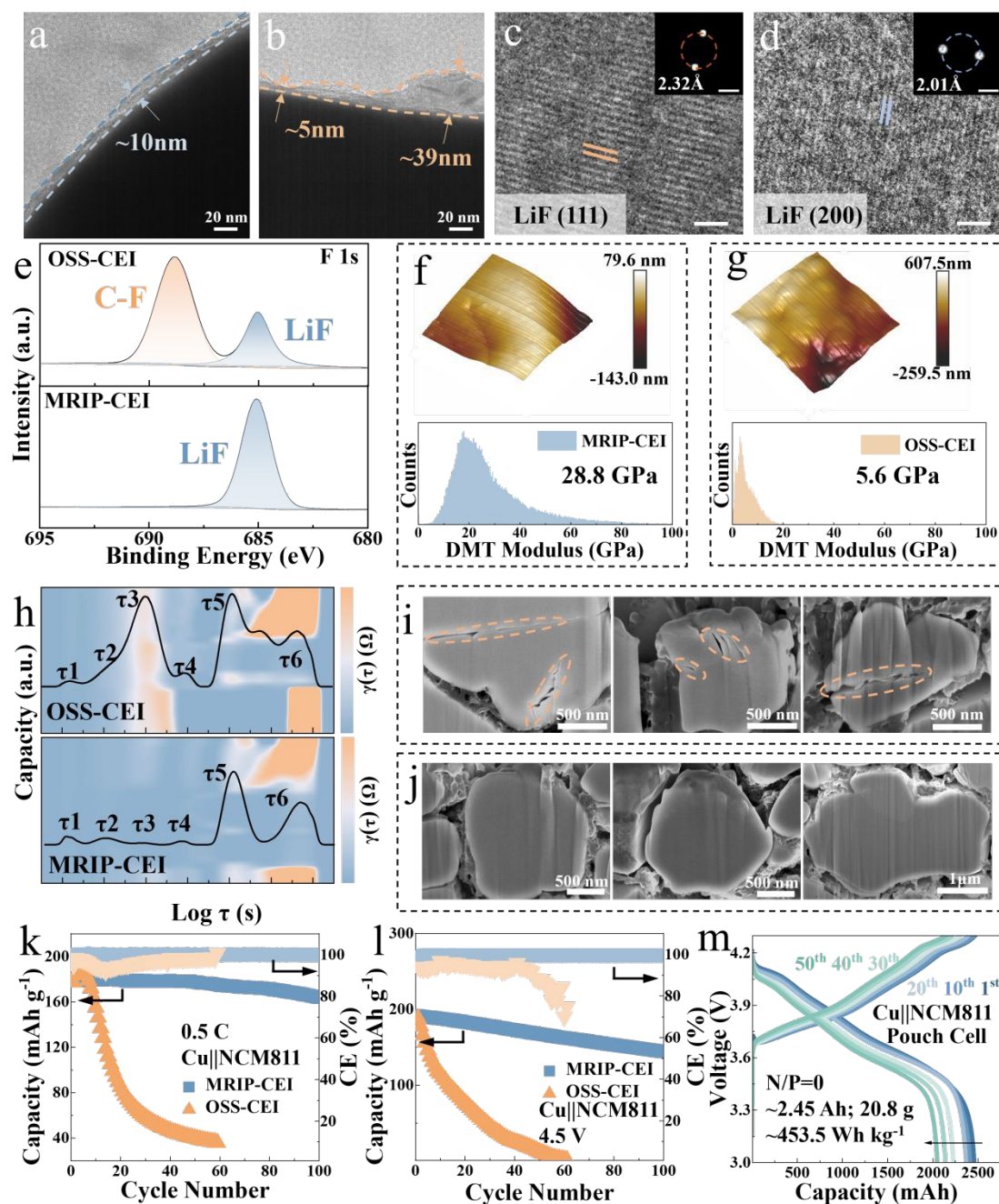
(Fig. 7i,j).

Fig. 7 MRIP-CEI to enhance cathode stability for anode-free Cu||NCM811 batteries. Cryo-TEM images of CEI morphology with (a) MRIP-CEI and (b) OSS-CEI. (c, d) High-resolution Cryo-TEM images of CEI morphology of MRIP-CEI (Scale bar: 1 nm; 5 1/nm). (e) XPS spectra of F 1s of MRIP-CEI and OSS-CEI. AFM images and DMT modulus distribution of (f) MRIP-CEI and (g) OSS-CEI. (h) Contour plots of the corresponding DRT results for the NCM811 cell with MRIP-CEI and OSS-CEI during charging/discharging processes. FIB-SEM images of NCM811 particles after cycling tests with (i) OSS-CEI and (j) MRIP-CEI. (k) Cycling performance of Cu||NCM811 full cells. (l) Cycling performance of anode-free Cu||NCM811 cells at 0.5C with a cut-off voltage of 4.5 V. (m) Charging/discharging curves of

anode-free Cu‖NCM811 pouch cell.

MRIP-CEI combines rapid ion diffusion capabilities with strong mechanical stability, enabling the high-nickel NCM811 cathode material to operate stably under high-voltage conditions in ether electrolyte with BTFE as the baseline additive (Fig. S42, Supporting Information). The NCM811 pouch cell (~760 mAh) with MRIP-CEI exhibits minimal capacity decay over 1000 cycles, with a fading rate of only 0.007% per cycle (Fig. S43, Supporting Information). Further practical validation in a full-cell configuration demonstrated outstanding performance. As shown in Fig. 7k and Fig. S44-S45, the Cu‖NCM811 full cell with MRIP-CEI achieves 91.6% capacity retention over 100 cycles, instead of the 25.2% of Cu@Ni‖NCM811 cell (after 50 cycles) and 12.4% of Cu‖NCM811 cell (after 15 cycles) with OSS-CEI. In addition, when cycled up to 4.5 V, the Cu‖NCM811 cell with MRIP-CEI delivers a specific discharge capacity exceeding 190 mAh g^{-1}, while still maintaining over 75% capacity retention after 100 cycles (Fig. 7l). Notably, the 2.45 Ah-level anode-free Cu‖NCM811 pouch cell design achieves stable cycling for over 50 cycles and delivers an energy density of 453.5 Wh kg^{-1} (Fig. 7m).

Conclusion

In summary, we propose a straightforward and effective strategy for developing anode-free lithium metal batteries through surface modification by helical counter-directional migration-induced anion-derived solvation sheaths. During the formation process, the ILF effect optimizes the migration pathways and association/dissociation behavior of electrolyte ions, directing anions to concentrate in the solvation structure of counter-migrating lithium ions. This innovative approach enables the formation of a robust SEI layer characterized by an ordered inorganic particle skeleton filled with organic components, which combines high mechanical strength and rapid ion permeability. This synergistic interaction facilitates favorable interfacial reactions, ultimately establishing a durable electrode-electrolyte interphase. The modified Cu electrode demonstrates an outstanding CE of 99.9%, and the lithium symmetric battery operated stably for more than 5,000 hours. The anode-less (N/P=0.8) lithium-metal full

cells maintain over 80% capacity retention after 1,000 stable cycles, and the capacity retention of anode-free Cu||LFP cell with MRIP-SEI is higher than 80% after 200 cycles. Notably, the HCMASS simultaneously optimizes the CEI layer through ILF and IEF driving, enabling stable operation of NCM811 cathodes in ether-based electrolytes. Anode-free Cu||NCM811 cells cycled in ether-based electrolyte at 4.5 V exhibit a capacity retention exceeding 75% after 100 cycles and realize a 453.5 Wh kg^{-1} anode-free lithium metal pouch cell configuration. Our work establishes a practical pathway for developing high-energy-density anode-free lithium metal batteries through this simple yet effective interfacial engineering approach.

Experimental

Materials

The lithium metal anodes were obtained from China Energy Lithium Co., Ltd. Lithium iron phosphate ($LiFePO_4$, LFP), Lithium Nickel Cobalt Manganese Oxide ($LiNi_{0.8}Co_{0.1}Mn_{0.1}O_2$, NCM811) cathodes, the ether-based electrolyte of 1.2 M LiTFSI-1,3-dioxolane (DOL)/1,2-Dimethoxyethane (DME) (vol/vol=1)-1%$LiNO_3$ and 1.2 M LiFSI-DOL/DME/ethylene glycol dibutyl ether (EGDBE)/bis(2,2,2-trifluoroethyl) ether (BTFE)-1% $LiNO_3$ were procured from Kelude Corporation, with all materials incorporated into the electrolytes within an argon-filled glovebox maintaining strict atmospheric control ($H_2O < 0.1$ ppm, $O_2 < 0.1$ ppm). Cu foils with different nickel layer thicknesses obtained by electroplating. Neodymium Iron Boron was used as magnetic field generator.

Electrochemical Measurement

Electrochemical measurements of Li||Cu cells

All electrochemical evaluations were performed using two-electrode CR2032 coin cells. Li||Cu cells were assembled to assess the cycling performance, conduct electrochemical analysis, and characterize morphological evolution. CE was evaluated via two independent methods: the conventional CE test and the Aurbach method.[32] Prior to cell assembly, copper current collectors were modified by attaching metal particles

of different morphologies. To prevent direct reduction of the silver initiator on the lithium metal surface, a passivation layer was pre-coated on the counter electrode. For comprehensive electrochemical characterization (EIS and LSV), Cu@Li electrodes were prepared by pre-depositing 0.5 or 1.0 mAh cm^{-2} of lithium onto copper substrates at a current density of 0.1 mA cm^{-2}. Symmetric cell cycling was carried out at current densities of 1.0 or 2.0 mA cm^{-2}. Electrochemical measurements (EIS, CV) were conducted on a CHI660E/760E electrochemical workstation (Shanghai Chenhua). EIS spectra were collected over a frequency range of 0.1 Hz to 10^5 Hz at temperatures between 30 and 60 °C, and the resulting impedance data were analyzed using Zview software to extract interfacial diffusion parameters. CV measurements were performed at a scan rate of 10 mV s^{-1} within a potential window of -0.2 to 0.2 V.

The interfacial diffusion activation energy based on the temperature-dependent EIS results was calculated using the Arrhenius equation:

$$\frac{T}{R_{in}} = Ae^{(-E_a/RT)}$$

where R_{in} is the ion transfer resistance of interface, T is the temperature, A is the pre-exponential constant, E_a is the activation energy of Li$^+$ diffusion when transporting through interface, and R is the standard gas constant. the Tafel plots of all samples were probed and obtained from the CV profiles. The exchange current (j_0) was calculated from the corresponding Tafel plots to reflect charge-transfer kinetics in Various SEIs. The process began by extracting the overpotential (η) and current density (j) data. The analysis relies on the Butler-Volmer equation. For the primary Tafel analysis, the data at higher overpotentials (where the system displays mixed kinetic-control) was plotted as η versus log $|j|$. The linear portions of these curves were fitted to the Tafel equation,

$$log\ |j| = log\ |j_0| \pm \frac{(1-\alpha)nF}{2.303RT}\eta$$

where j_o denotes the exchange current density, α represents the charge transfer coefficient, F is the Faraday constant, R indicates the gas constant, and T is the absolute temperature.

The porosity (P) of the Li deposit was then determined by calculating the volume

fraction occupied by voids, derived from the ratio of the theoretical (d_t) to actual thickness (d_a):

$$P(\%) = \left(1 - \frac{d_t}{d_a}\right) \times 100\%$$

where the d_a was directly obtained from statistical analysis of the FIB-SEM images, d_t is obtained from the theoretical density and capacity of lithium metal.

Full cells assembly and electrochemical measurements

Cu‖LFP coin cells were employed to evaluate rate capability and cycling performance at various rates. Pouch cells were used to study anode-free full cells. NCM811 (96.7% active materials, ~22 mg cm^{-2}) was used as the cathode material, and bare Cu (8 μm) was used as the anode current collector. The pouch cells were filled with 2.0 g liquid electrolyte before being vacuum sealed. The pouch cells were cycled at 0.1 C charge and discharge between 2.8 V and 4.3 V after the initial activation, at a 0.5 C charge-discharge rate. The total pouch cell capacity was about 2.5 Ah under these conditions. In addition, a 0.8 Ah pouch cell with graphite anode and NCM811 cathode was assembled.

The DRT analysis was employed to deconvolve the overlapping electrochemical processes in the measured in-situ EIS data of the Li‖NCM811 cell. Regarding the specific data acquisition process, DRT was indeed calculated using a well-established and publicly available MATLAB toolbox developed by Cucci research group[33]. The process involved importing the raw EIS data directly into this specialized software. The resulting DRT plot, which presents the polarization resistance as a distribution of relaxation times, was then used to identify the characteristic frequencies of the various electrochemical processes based on their well-documented time constants in literature[34].

Characterizations

The Cryo-TEM characterization was performed on Thermo Scientific Glacios cryo-TEM microscope operated at 200 keV to analyze the composition and structure of SEI. ToF-SIMS (IonTof M6 Hybrid) was also investigated SEI components. AFM (Dimension ICON) was used to analysis the DMT modulus. In-situ Raman spectra was

performed under 785 nm laser excitation (Invia). The morphology of the deposited Li was determined by an extremely high-resolution scanning electron microscope (SEM, JSM 7800F, JEOL). The operation voltage of the SEM was 10.0 kV or 15.0 kV. The morphology of lithium deposition/stripping and the integrity of SEI were explored by SEM after long-term cycles. The cross-section morphology was determined by focused ion beam-scanning electron microscope (FEI Helios G4 UX). A rough cross-sectional milling (30 kV, 1000 pA) was done on the anode by the FIB (Ga beam). XPS measurements were performed with a Surface Analysis Kratos Axis Supra+ to investigate the chemical compositions of the plating electrodes. The samples were transferred into the XPS machine under vacuum using an air-tight sample holder.

First-principles computation

The computational work was performed using the VASP software package with the GGA-PBE functional. Spin-polarized calculations were conducted with a plane-wave cutoff energy of 450 eV, energy convergence criteria of 10^{-6} eV, and force convergence threshold of -0.05eV Å^{-2}. 15 Å vacuum layer was applied along the z-axis to mitigate periodic boundary effects. The Cu (200) surface model (10.22Å × 10.22Å × 19.17Å) contained 48 Cu atoms with 3×3×1 k-point sampling. Similarly, the Ni (111) surface (11.56 Å × 11.56 Å × 19.72 Å) comprised 48 Ni atoms with equivalent k-point settings. The adsorption energies (Eads) of TFSI$^-$ on the substrates were calculated as follows:

$$E_{ads} = E_{Li+sur} - E_{aur} - E_{Li}$$

Where the E_{sur} and E_{Li+sur} are the structural total energies of studied system before and after Li surface absorption, E_{Li} is the system energy of lithium.

COMSOL simulation

A simplified two-dimensional model was established to investigate lithium deposition morphologies on substrates with varying densities of active nucleation sites. The model couples the Butler-Volmer equation for electrochemical kinetics at the electrode surface with Fick's law for ion concentration diffusion and the Nernst-

Einstein relationship for ion migration. The simulation domain, set to $50 \times 25 \ \mu m^2$, was discretized using a fine triangular mesh. A comparative analysis was performed across substrates with differing numbers of active sites to elucidate their influence.

For the exploration of helical migration, in terms of the computational domain and electrodes, the overall model was a cylinder. The top is a flat circular lithium metal electrode, serving as the emission source of lithium ions. The bottom was a copper electrode, designed with a central protrusion. This protrusion was used to alter the electric field distribution in the bottom space, thereby simulating the effect of microscopically rough electrode surfaces on ions motion. The space between the two electrodes was filled with an electrolyte medium. The main simulation workflow includes: Initialization: Set the initial position and initial velocity (typically zero or a very small random value) of the particles on the surface of the top lithium electrode; Time stepping: For each particle, apply the RK4 method to iteratively update its position and velocity; Termination check: After each iteration step, check the following termination conditions; Particle reaches the collector: When the distance between the particle and the surface of the bottom copper electrode is less than a set threshold, the particle is considered successfully collected, and its trajectory and time of flight are recorded.

MD simulation

MD simulations were carried out using the Forcite module within the Materials Studio software package (2020 release) to investigate the role of M-Ni in modulating the solvation sheath structure. The simulation system was constructed to closely mimic experimental conditions. Initially, molecules were randomly packed into a cubic box with dimensions of 60 Å along the x, y, and z axes. After pre-equilibration in the isothermal-isobaric (NPT) ensemble, the box size stabilized at 56.3 Å. All MD simulations employed the COMPASS II (Condensed-phase Optimized Molecular Potentials for Atomistic Simulation Studies II) forcefield, which is suitable for systems comprising both organic and inorganic components and accurately reproduces the

structure and properties of condensed phases, making it well-suited for modeling the electrolyte system under study. Electrostatic interactions were treated using the particle–particle particle-mesh (PPPM) method.

Acknowledgements

Author information

Y.C. and M.S. conceived the concept and the project. Y.C. conducted all experiments, measurements, and calculations. Y.L., X.Q., Y.Q., Y.T.K., S.Z., X.L., and S.L. were involved in the discussions. All authors participated in the analysis of the results and reviewed the manuscript.

Ethics declarations

Competing interests

The authors declare no competing interests.

Supplementary information

Supplementary Figs. 1-45 and Tables 1-3.

References

1. I. R. Choi, Y. Chen, A. Shah, J. Florian, C. Serrao, J. Holoubek, H. Lyu, E. Zhang, J. H. Lee, Y. Lin, S. C. Kim, H. Park, P. Zhang, J. Lee, J. Qin, Y. Cui and Z. Bao, *Nat. Energy*, 2025, **10**, 365-379.
2. Y. Lu, Q. Cao, W. Zhang, T. Zeng, Y. Ou, S. Yan, H. Liu, X. Song, H. Zhou, W. Hou, P. Zhou, N. Hu, Q. Feng, Y. Li and K. Liu, *Nat. Energy*, 2025, **10**, 191-204.
3. C. Jin, Y. Huang, L. Li, G. Wei, H. Li, Q. Shang, Z. Ju, G. Lu, J. Zheng, O. Sheng and X. Tao, *Nat. Commun.*, 2023, **14**, 8269.
4. Y. Xia, P. Zhou, X. Kong, J. Tian, W. Zhang, S. Yan, W.-h. Hou, H.-Y. Zhou, H. Dong, X. Chen, P. Wang, Z. Xu, L. Wan, B. Wang and K. Liu, *Nat. Energy*, 2023, **8**, 934-945.

5. M. Mao, X. Ji, Q. Wang, Z. Lin, M. Li, T. Liu, C. Wang, Y.-S. Hu, H. Li, X. Huang, L. Chen and L. Suo, *Nat. Commun.*, 2023, **14**, 1082.

6. J. Shi, T. Koketsu, Z. Zhu, M. Yang, L. Sui, J. Liu, M. Tang, Z. Deng, M. Liao, J. Xiang, Y. Shen, L. Qie, Y. Huang, P. Strasser and J. Ma, *Nat. Mater.*, 2024, **23**, 1686-1694.

7. T. Fuchs, T. Ortmann, J. Becker, C. G. Haslam, M. Ziegler, V. K. Singh, M. Rohnke, B. Mogwitz, K. Peppler, L. F. Nazar, J. Sakamoto and J. Janek, *Nat. Mater.*, 2024, **23**, 1678-1685.

8. Q. Xu, T. Li, Z. Ju, G. Chen, D. Ye, G. I. N. Waterhouse, Y. Lu, X. Lai, G. Zhou, L. Guo, K. Yan, X. Tao, H. Li and Y. Qiu, *Nature*, 2025, **637**, 339-346.

9. K. Huang, S. Bi, B. Kurt, C. Xu, L. Wu, Z. Li, G. Feng and X. Zhang, *Angew. Chem., Int. Ed.*, 2021, **133**, 19381-19389.

10. S. Jurng, Z. L. Brown, J. Kim and B. L. Lucht, *Energy Environ. Sci.*, 2018, **11**, 2600-2608.

11. P. Liu, S. Shen, Z. Qiu, T. Yang, Y. Liu, H. Su, Y. Zhang, J. Li, F. Cao and Y. Zhong, *Adv. Mater.*, 2024, **36**, 2312812.

12. S. Kim, J. H. Jeon, K. Park, S. H. Kweon, J.-H. Hyun, C. Song, D. Lee, G. Song, S.-H. Yu, T. K. Lee, S. K. Kwak, K. T. Lee, S. Y. Hong and N.-S. Choi, *Adv. Mater.*, 2024, **36**, 2401615.

13. J. Liu, W. Hao, M. Fang, X. Chen, Y. Dong, Y. Chen, Z. Wang, X. Yue and Z. Liang, *Nat. Commun.*, 2024, **15**, 9356.

14. W. Liu, T. Xie, X. Wang, W. Deng, L. Huang, R. Khan, Y. Wang, H. Hou, D. Wang and Y. Wu, *Adv. Funct. Mater.*, 2024, **34**, 2410843.

15. H. Song, J. Lee, M. Sagong, J. Jeon, Y. Han, J. Kim, H.-G. Jung, J.-S. Yu, J. Lee and I.-D. Kim, *Adv. Mater.*, 2024, **36**, 2407381.

16. F. Zhao, P. Zhai, Y. Wei, Z. Yang, Q. Chen, J. Zuo, X. Gu and Y. Gong, *Adv. Sci.*, 2022, **9**, 2103930.

17. Y. Chen, X. Dou, K. Wang and Y. Han, *Adv. Energy Mater.*, 2019, **9**, 1900019.

18. Y. Chen, H. Huang, L. Liu, Y. Chen and Y. Han, *Adv. Energy Mater.*, 2021, **11**, 2101774.

19. Y. Chen, Y. Chen, R. Wang, X. Lv and Y. Han, *Chem. Eng. J.*, 2022, **446**, 137435.

20. Y. Chen, H. Liu, L. Liu, J. Li and Y. Han, *Batteries & Supercaps*, 2024, **7**, e202300389.

21. J. Holoubek, H. Liu, Z. Wu, Y. Yin, X. Xing, G. Cai, S. Yu, H. Zhou, T. A. Pascal, Z. Chen and P. Liu, *Nat. Energy*, 2021, **6**, 303-313.

22. S. Zhu and J. Chen, *Energy Storage Mater.*, 2022, **44**, 48-56.

23. Q. Li, G. Liu, Y. Chen, J. Wang, P. Kumar, H. Xie, W. Wahyudi, H. Yu, Z. Wang, Z. Ma and J. Ming, *Adv. Funct. Mater.*, 2025, **35**, 2420327.

24. X. Wang, M. Chen, S. Li, C. Zhao, W. Zhang, Z. Shen, Y. He, G. Feng and Y. Lu, *ACS Cent. Sci.*, 2021, **7**, 2029-2038.

25. D. Huang, C. Zeng, M. Liu, X. Chen, Y. Li, J. Zou, Q. Pan, F. Zheng, H. Wang and Q. Li, *Small*, 2025, 2412259.

26. P. Zhai, Q. He, H. Jiang, B. Gao, B. Zhang, Q. Chen, Z. Yang, T. Wang and Y. Gong, *Adv. Energy Mater.*, 2024, **14**, 2302730.

27. H. Zhuang, H. Xiao, T. Zhang, F. Zhang, P. Han, M. Xu, W. Dai, J. Jiao, L. Jiang and Q. Gao, *Angew. Chem., Int. Ed.*, 2024, **63**, e202407315.

28. S. Liu, X. Ji, N. Piao, J. Chen, N. Eidson, J. Xu, P. Wang, L. Chen, J. Zhang, T. Deng, S. Hou, T. Jin, H. Wan, J. Li, J. Tu and C. Wang, *Angew. Chem., Int. Ed.*, 2021, **60**, 3661-3671.

29. H. Liu, F. Zhen, X. Yin, Y. Wu, K. Yu, X. Kong, S. Ding and W. Yu, *Angew. Chem., Int. Ed.*, 2025, **64**, e202414599.

30. J. Xiao, *Science*, 2019, **366**, 426-427.

31. A. Jana, S. I. Woo, K. S. N. Vikrant and R. E. García, *Energy Environ. Sci.*, 2019, **12**, 3595-3607.

32. T. Ma, Y. Ni, Q. Wang, W. Zhang, S. Jin, S. Zheng, X. Yang, Y. Hou, Z. Tao and J. Chen, *Angew. Chem., Int. Ed.*, 2022, **134**, e202207927.

33. T. H. Wan, M. Saccoccio, C. Chen and F. Ciucci, *Electrochim. Acta*, 2015, **184**, 483-499.

34. Y. Lu, C.-Z. Zhao, J.-Q. Huang and Q. Zhang, *Joule*, 2022, **6**, 1172-1198.

Data Availability Statement

The data that support the findings of this study are available from the corresponding

author on reasonable request.